


ORIGINAL RESEARCH

Open Access



# Analysis of low voltage ride-through capability and optimal control strategy of doubly-fed wind farms under symmetrical fault

Botong Li<sup>1,2\*</sup> , Dingchuan Zheng<sup>1,2</sup>, Bin Li<sup>1,2</sup>, Xinru Jiao<sup>1,2</sup>, Qiteng Hong<sup>3</sup> and Liang Ji<sup>4</sup>

## Abstract

Given the “carbon neutralization and carbon peak” policy, enhancing the low voltage ride-through (LVRT) capability of wind farms has become a current demand to ensure the safe and stable operation of power systems in the context of a possible severe threat of large-scale disconnection caused by wind farms. Currently, research on the LVRT of wind farms mainly focuses on suppressing rotor current and providing reactive current support, while the impact of active current output on LVRT performance has not been thoroughly discussed. This paper studies and reveals the relationship between the limit of reactive current output and the depth of voltage drop during LVRT for doubly-fed induction generator (DFIG) based wind farms. Specifically, the reactive current output limit of the grid-side converter is independent of the depth of voltage drop, and its limit is the maximum current allowed by the converter, while the reactive current output limit of the DFIG stator is a linear function of the depth of voltage drop. An optimized scheme for allocating reactive current among the STATCOM, DFIG stator, and grid-side converter is proposed. The scheme maximizes the output of active current while satisfying the standard requirements for reactive current output. Compared to traditional schemes, the proposed LVRT optimization strategy can output more active power during the LVRT period, effectively suppressing the rate of rotor speed increase, and improving the LVRT performance and fault recovery capability of wind farms. Simulation results verify the effectiveness of the proposed scheme.

**Keywords** Doubly-fed induction generator (DFIG), Low voltage ride-through (LVRT), Transient characteristics, Reactive current output capacity, Maximum active power

## 1 Introduction

According to the data from the International Energy Agency, the total consumption of fossil fuels and renewable energy has been increasing over the past 10 years. However, renewable energy has experienced more significant development and growth. Because of the increasing concerns of countries on energy shortages, ecological environmental pollution, and climate change, the development of renewable energy is expected to further accelerate in the future, while the consumption of fossil fuels will tend to stabilize or even decrease [1]. Among renewable energies, wind power has received significant attention and development. According to the Statistical

\*Correspondence:

Botong Li  
[libotong@tju.edu.cn](mailto:libotong@tju.edu.cn)

<sup>1</sup> Key Laboratory of Smart Grid of Ministry of Education, Tianjin University, Tianjin 300072, China

<sup>2</sup> National Industry-Education Platform of Energy Storage, Tianjin University, Tianjin 300072, China

<sup>3</sup> Department of Electronic and Electrical Engineering, University of Strathclyde, Glasgow G1 1XQ, UK

<sup>4</sup> Department of Electrical Power Engineering, Shanghai University of Electric Power, Shanghai 200090, China

Bulletin of National Economic and Social Development of the People's Republic of China, the installed capacity of wind power in China has increased from 60.83 to 328.48 GW in the past 10 years, and its proportion of installed capacity for power generation has increased from 5.31 to 13.81%. In 2020, China officially proposed the strategic goal of "carbon peak by 2030 and carbon neutrality by 2060". It is expected that wind power technology in China will continue to be developed, and the proportion of wind power installed capacity will be further increased, making wind energy an important component of China's energy industry.

There are two main types of wind turbines: those based on doubly-fed induction generators (DFIG) and those using permanent magnet synchronous generators (PMSG). The converter capacity of a DFIG is only 30–35% of the rated generator capacity, which has low cost and power loss, so it is widely used in onshore wind farms [2–5]. However, the stator of a DFIG is directly connected to the power grid and when the external power grid fails, the stator flux will generate a large transient component, causing severe overvoltage and overcurrent on the rotor side of the DFIG [6–8]. If no protective measures are taken, the converter could be damaged [9], directly affecting the safety and stable operation of the power system [10]. Therefore, the latest GB/T 19963.1-2021 standard in China requires that wind farms should have low voltage ride-through (LVRT) capability, i.e., during the voltage drop period, wind turbines can maintain continuous operation without disconnection from the grid for a period of time, and at the same time inject reactive current into the grid to support voltage recovery [11–14].

DFIG-based wind turbines are generally equipped with crowbar protection circuits to achieve LVRT. In traditional schemes, the crowbar protection device will be put into operation when the voltage at the point of common coupling (PCC) drops, and then be removed after the fault is cleared. This approach ensures that the electrical quantities of the wind turbine system remain within limits to achieve fault ride-through. However, the converter cannot effectively control the DFIG during the activation of the crowbar protection. Consequently, the DFIG operates asynchronously and absorbs a significant amount of reactive power from the grid, which further exacerbates the voltage drop [15–17]. Considering the deficiency of the traditional crowbar protection scheme in reactive power compensation, a lot of research on DFIG LVRT methods has been carried out and many achievements obtained. Reference [18] relies on the expression of rotor current after the insertion of the crowbar to propose a dynamic crowbar resistance adjustment method to effectively suppress rotor overcurrent and reduce the crowbar protection activation time. In [19], a new crowbar

protection structure, consisting of a resistor and a capacitor in series, is proposed to reduce the reactive power absorbed by the DFIG from the grid during the crowbar insertion period. At the same time, reactive power support is provided by the grid-side converter (GSC), meeting the reactive power demand in scenarios where the voltage drop is small. In [20], through time-domain analysis, the electrical characteristics of DFIG rotor current and voltage under symmetrical faults are revealed, and it points out that rotor current can be reduced by increasing the DC voltage of the converter, increasing the transient rotor-side inductance, and reducing the induced electromotive force. By introducing a virtual resistance in the rotor-side converter (RSC) control loop in [21], the equivalent rotor-side resistance is increased, the decay of stator magnetic flux is accelerated, and the rotor current is effectively suppressed. This expands the uninterrupted operational region of the DFIG. In [22], during symmetrical faults in the grid, the RSC is used to simulate inductance to limit the rotor voltage and current within the allowable range of the RSC, ensuring the controllability of the system during transient processes. By using virtual capacitance compensation to suppress the free oscillation of the stator magnetic flux and the rotor current in [23], the LVRT capability of the DFIG wind farm is improved, whereas reference [24] proposes a scheme to switch off and restart the RSC after 40 ms of crowbar protection activation, and to control the stator to provide reactive current support to the grid by switching the RSC current loop reference value. However, the paper does not consider the reactive power output capability of the DFIG, and it remains to be verified whether the RSC can meet the demand in scenarios with large voltage drops. In [25], the reactive power output capability of the DFIG stator and the GSC is analyzed, and a scheme is proposed to prioritize the injection of reactive power into the grid from the stator. This scheme provides a feasible method for injecting reactive power, but whether it is the optimal allocation scheme requires further exploration. In [26, 27], reactive power is injected into the grid during external grid faults by using a static synchronous compensator (STATCOM) and static var compensator (SVC), to increase the DFIG terminal voltage and improve the LVRT capability of the wind farm. This scheme does not use the reactive power output capability of the wind turbines and requires a large capacity from reactive power compensation devices. The dynamic voltage restorer (DVR) is connected in series between the wind farm and the grid in [28] to compensate for the voltage drop at the DFIG stator during faults and eliminate the impact of voltage drop on the PCC of the wind farm. While based on the principle of DVR, reference [29] proposes a series-coupled compensation device to reduce the degree of

voltage drop in the wind farm and improve the LVRT capability. However, this scheme requires additional equipment and has higher costs. The studies in [18–23] effectively suppress the rotor-side current, protect the wind turbine converter, and achieve the control objective of keeping the wind turbine connected to the grid during the LVRT period. Although they reduce the reactive power absorbed from the grid to a certain extent, they still cannot meet the goal of reactive current support. Studies in [24–29] which are related to reactive power compensation during the LVRT period of wind farms mainly focus on relying solely on either the wind turbine or a reactive compensation device to provide reactive power support, while they lack coordination of the reactive power output between the DFIG stator, GSC and reactive compensation device.

While the existing research mainly focuses on the reactive power support of wind farms during grid faults, the impact of active current output on the LVRT performance has not received sufficient attention. GB/T 19963.1-2021 only specifies the reactive current output of wind turbines during LVRT without providing requirements or guidelines for active power output during this period. In fact, wind turbines entering LVRT control can easily lose a large amount of active power output, which may cause significant active power deficit in power systems with low inertia, leading to decrease in system frequency. In severe cases, it may trigger the operation of low-frequency load shedding devices or even lead to the collapse of the system frequency. Therefore, it is of great significance to fully use wind farms' regulation ability to reduce the active power shortage during LVRT and enhance the wind turbines' frequency support capability for the safe and stable operation of the grid. Additionally, the mechanical power input of the wind turbine can be approximated as constant during LVRT, while the electromagnetic power output of the DFIG decreases, resulting in power imbalance and increase in rotor speed. If the DFIG can output more active power during grid faults,

it can slow down the increase in rotor speed and effectively increase the recovery rate of active power output after voltage recovery. Overall, maximizing the output of active current during LVRT in wind farms is a more favorable operating mode.

This paper first analyzes the transient characteristics of the DFIG rotor under symmetrical faults, and then discusses the detailed relationship between the reactive current output limit of the DFIG stator and the GSC, and the depth of voltage drop. From this, a comprehensive LVRT optimization control strategy is proposed, one which considers the reactive and active power output of wind farm, depending on whether STATCOM is installed in the wind farm. Finally, the effectiveness of the proposed strategy is demonstrated through simulations on the PSCAD/EMTDC platform.

## 2 Characteristics of DFIG rotor side fault under symmetric failure

### 2.1 DFIG structure and control strategies

The DFIG-based wind turbine system includes a wind turbine, a DFIG, a grid-side converter, and a rotor-side converter. The crowbar protection circuit is installed on the AC side of the RSC, and the DC side is equipped with a chopper protection circuit to prevent overvoltage. Most wind farms are equipped with reactive power compensation devices such as STATCOM to enhance the LVRT capability. A typical DFIG wind turbine structure used in this study is shown in Fig. 1:

Figure 2 presents the control block diagram of the DFIG wind turbine converter. The control strategy of the GSC and RSC under normal operating conditions adopts the commonly used vector control strategy [30, 31]. The d-axis control objective of the GSC is the DC voltage ( $U_{dc}$ ), and the q-axis control objective is the reactive power ( $Q_g$ ) of the GSC. The d-axis control objective of the RSC is the stator active power ( $P_s$ ), whose reference value is obtained from maximum wind energy tracking, while the q-axis control objective is the stator output

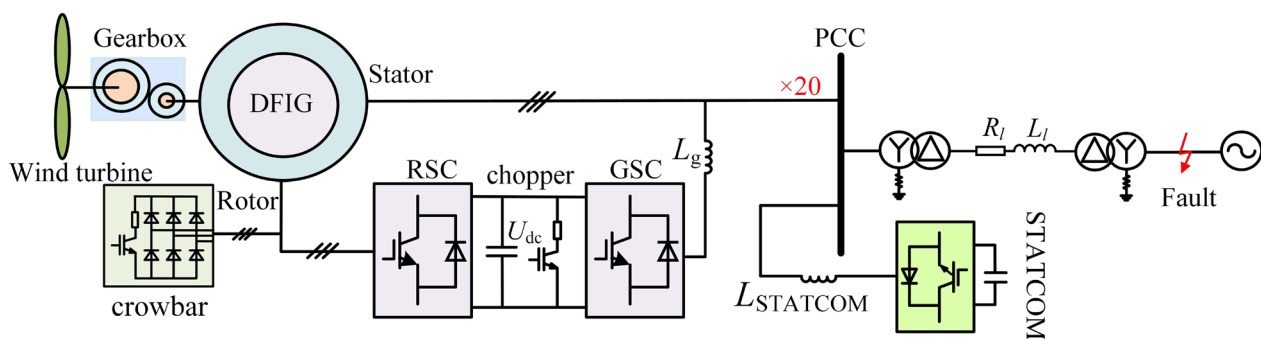


**Fig. 1** Structure diagram of DFIG wind turbine system

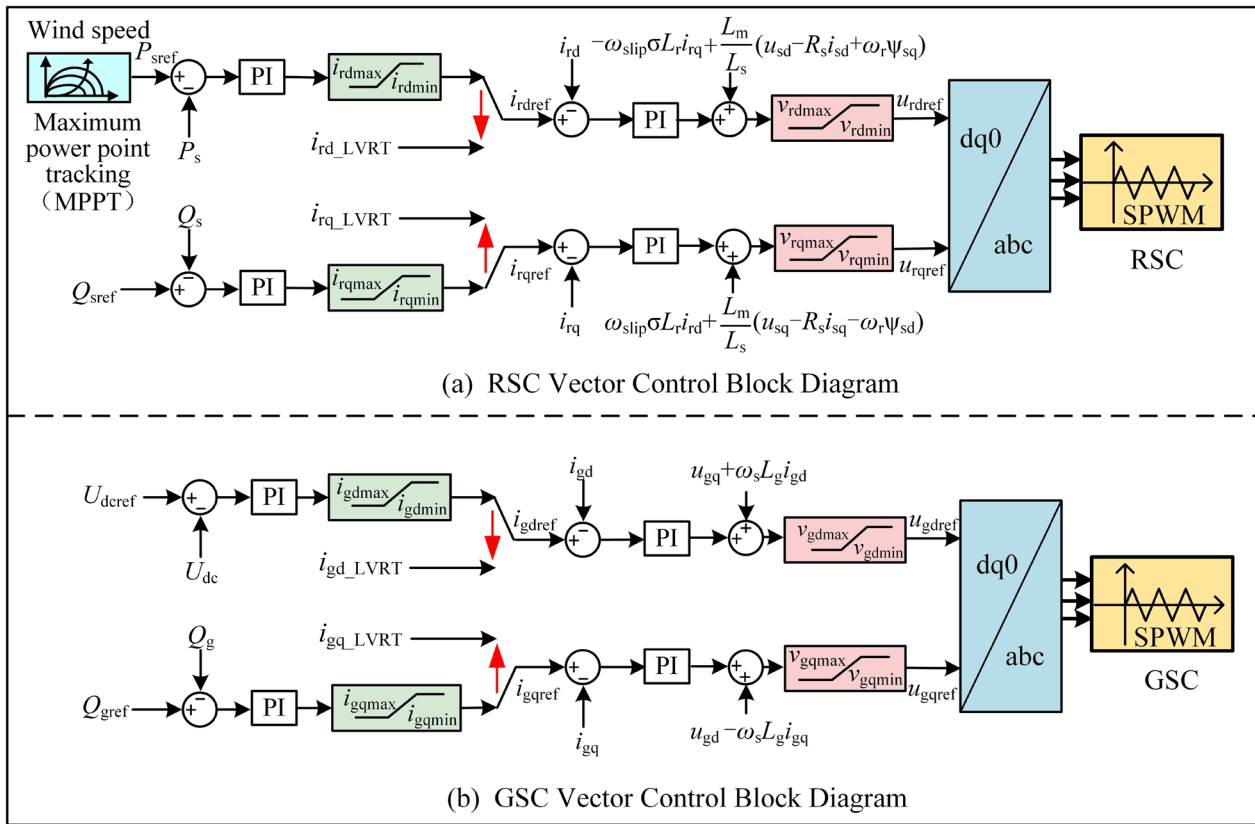


**Fig. 2** Control block diagram of the DFIG wind turbine converters

reactive power ( $Q_s$ ). During LVRT, the control system switches the current inner loop reference values according to requirements, which will be discussed and analyzed in Sect. 3.3.

## 2.2 DFIG mathematical model in rotor coordinate system

In the rotor rotating coordinate system, the vector form mathematical model of a DFIG can be expressed as [32]:

$$\begin{cases} \mathbf{U}_s^r = R_s \mathbf{I}_s^r + \frac{d\boldsymbol{\psi}_s^r}{dt} + j\omega_r \boldsymbol{\psi}_s^r \\ \mathbf{U}_r^r = R_r \mathbf{I}_r^r + \frac{d\boldsymbol{\psi}_r^r}{dt} \\ \boldsymbol{\psi}_s^r = L_s \mathbf{I}_s^r + L_m \mathbf{I}_r^r \\ \boldsymbol{\psi}_r^r = L_r \mathbf{I}_r^r + L_m \mathbf{I}_s^r \end{cases} \quad (1)$$

where  $\mathbf{U}$  and  $\mathbf{I}$  represent the voltage and current vectors, and  $R$  and  $L$  represent the resistance and inductance, respectively.  $\boldsymbol{\psi}$  represents the flux vector,  $\omega_r$  represents the rotor speed, and  $L_m$  represents the excitation inductance.

By substituting the flux equation in (1) into the rotor voltage equation, the rotor voltage vector can be obtained as:

$$\mathbf{U}_r^r = \left( R_r \mathbf{I}_r^r + \sigma L_r \frac{d\mathbf{I}_r^r}{dt} \right) + \frac{L_m}{L_s} \frac{d\boldsymbol{\psi}_s^r}{dt} \quad (2)$$

where  $\sigma$  is the magnetic leakage coefficient.

From (2), an equivalent circuit of DFIG rotor side can be obtained, as shown in Fig. 3.

The rotor electromotive force in Fig. 3 consists of two parts, i.e., one is the voltage drop generated by the rotor current in the equivalent impedance, corresponding to the first term in (2), and the other is the induced

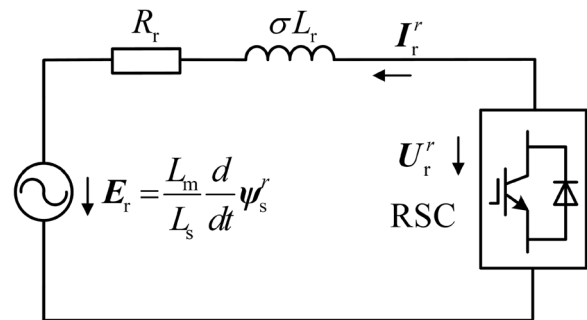


**Fig. 3** Equivalent circuit at the rotor side of DFIG

electromotive force  $E_r$  generated by the stator flux on the rotor side, corresponding to the second term in (2).

### 2.3 Transient characteristics of the rotor under symmetrical fault

Assuming a three-phase symmetrical fault occurs in the grid at  $t=0$ , and that the voltage drop depth at the PCC of the wind farm is  $h$ , there are [33]:

$$\mathbf{U}_s^r = \begin{cases} U_s e^{j(\omega_s - \omega_r)t} & t < 0 \\ (1-h)U_s e^{j(\omega_s - \omega_r)t} & t \geq 0 \end{cases} \quad (3)$$

where  $U_s$  is the grid voltage modulus during normal operation, and  $\omega_s$  is the synchronous speed.

In accordance with the principle of flux continuity, the stator flux remains unchanged immediately before and after the voltage drop. The stator flux will transition from the pre-fault steady state to a new steady state after the fault, and this transition process can be described by [34]:

$$\frac{d\psi_s^r}{dt} = \mathbf{U}_s^r - \frac{R_s}{L_s} \psi_s^r \quad (4)$$

From (4), the expression of stator flux can be obtained for  $t \geq 0$ , i.e.:

$$\psi_s^r = \frac{(1-h)U_s e^{j(\omega_s - \omega_r)t}}{j\omega_s} + \frac{hU_s}{j\omega_s} e^{-(1/\tau_s + j\omega_r)t} \quad (5)$$

where  $\tau_s = L_s/R_s$ ,  $\tau_s$  is the stator time constant.

Substituting (5) into (2), it can be seen that the induced electromotive force generated by the stator flux at the rotor side after voltage drop is:

$$\mathbf{E}^r = \frac{L_m}{L_s} \left[ s(1-h)U_s e^{j(\omega_s - \omega_r)t} - \left( \frac{1}{\tau_s} + j\omega_r \right) \frac{hU_s}{j\omega_s} e^{-(1/\tau_s + j\omega_r)t} \right] \quad (6)$$

where  $s$  represents slip rate as  $s = (\omega_r - \omega_s)/\omega_s$ .

Generally,  $L_s$  is much larger than  $R_s$ , resulting in a large value of  $\tau_s$ . Therefore, the term  $1/\tau_s$  in (6) can be ignored, and the maximum induced electromotive force ( $E_{rmax}$ ) on the rotor side due to the stator flux can be expressed as:

$$|E_{rmax}| \approx \frac{L_m}{L_s} (|s|(1-h)U_s + (1-s)hU_s) \quad (7)$$

The slip rate  $s$  is generally within  $\pm 0.3$  during normal operation of the DFIG. Figure 4 shows the maximum induced electromotive force ( $E_{rmax}$ ) with different levels of voltage drop. As shown, SPWM represents the maximum output voltage of the RSC under SPWM modulation, i.e.  $U_{dc}/2$ , whereas SVPWM represents the maximum output voltage of the RSC under SVPWM modulation, which is  $U_{dc}/\sqrt{3}$ .

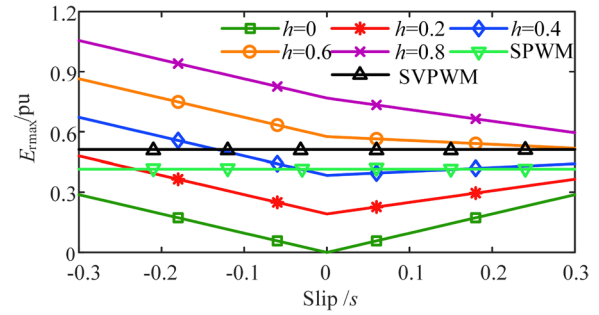


Fig. 4 Induced electromotive force at rotor side

When the DFIG operates normally ( $h=0$ ), the induced electromotive force on the rotor side only contains a steady-state component, which is small and can be effectively controlled by the RSC. However, when the voltage drop depth is large, the free component of the stator flux will induce a large electromotive force on the rotor side. Because of the limitation of the DC voltage, the output voltage of the RSC is insufficient to offset the induced electromotive force. In addition, the small rotor resistance and magnetic leakage coefficient will cause over-current at the rotor side when the voltage drop depth is large.

### 3 Low voltage ride-through method for a DFIG wind farm

#### 3.1 LVRT performance requirements of the wind turbine

According to China's latest national standard GB/T 19963.1-2021 "Technical Regulations for Wind Farm Access to Power System Part 1: Onshore Wind Power", wind turbines should meet various requirements during the LVRT period.

GB/T 19963.1-2021 requires wind turbines to operate continuously without disconnection when the voltage at the PCC of the wind farm is in Area A, while the wind turbines are allowed to disconnect when the voltage at the PCC of the wind farm is in Area B, as shown in Fig. 5. At the same time, the wind farm should have dynamic reactive power support capability during the LVRT period, and the injected dynamic reactive current increment ( $\Delta I_q$ ) should meet:

$$\Delta I_q = K \times (0.9 - U_{pcc}) \times I_N, (0.2 \leq U_{pcc} \leq 0.9) \quad (8)$$

where  $K$  is the reactive compensation coefficient ( $1.5 \leq K \leq 3$ ),  $U_{pcc}$  is the per unit value of the PCC, and  $I_N$  is the rated current of the wind farm.

The current standard does not further limit the value of  $K$ . In fact, different wind farms have different reactive current output capacities. For wind farms



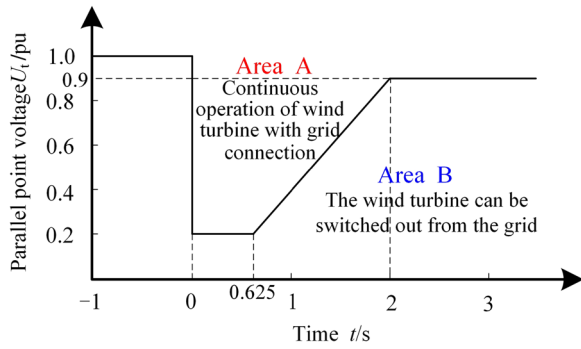


**Fig. 5** Requirements for LVRT of Wind Farms

equipped with STATCOM or other reactive compensation devices, the reactive compensation capacity is high, and the reactive compensation coefficient  $K$  can be increased according to the output reactive current capacity of the STATCOM and the wind turbines. In contrast, wind farms without a reactive compensation device can only rely on the wind turbines so the reactive power compensation capability is weak. Thus, the reactive power compensation coefficient  $K$  is relatively small.

### 3.2 Analysis of reactive power support capacity of a DFIG during the LVRT period

The reactive current output capability of the DFIG system comes from two aspects, i.e., the GSC and the DFIG stator. The reactive current output limits of these two parts are analyzed below.

#### (1) Reactive current output capacity of the GSC.

If the maximum allowable current amplitude of the GSC is  $I_{gmax}$ , the grid voltage amplitude is  $U_s$  during normal operation, the voltage drop depth during fault is  $h$ , the active power output of the GSC during fault is  $P_g$ , and the reactive power output is  $Q_g$ . The power constraint during the fault is:

$$P_g^2 + Q_g^2 \leq ((1-h)U_s I_{gmax})^2 \quad (9)$$

The relationship between the active power of the GSC and the total output power of the DFIG ( $P_{DFIG}$ ) is shown as [35]:

$$P_g = \frac{-s}{1-s} P_{DFIG} \quad (10)$$

From (9) and (10), when the total output active power of the DFIG is 0, the output reactive power of the GSC is the highest, and thus there are:

$$\begin{cases} Q_{gmax} = (1-h)U_s I_{gmax} \\ i_{gqmax} = \frac{Q_{gmax}}{(1-h)U_s} = I_{gmax} \end{cases} \quad (11)$$

It can be seen that the reactive current output limit ( $i_{gqmax}$ ) of the GSC is related to the allowed maximum current ( $I_{gmax}$ ) passing through the converter. Generally, the slip rate  $s$  of the DFIG system is between  $-0.3$  and  $0.3$ , while the converter capacity is generally designed according to the maximum slip rate  $s_{max}$ . Thus,  $I_{gmax}$  is usually  $0.3$  pu, and therefore, the maximum reactive current output  $i_{gqmax}$  of the GSC is  $0.3$  pu.

#### (2) DFIG stator reactive current output capacity.

DFIG control strategies mostly adopt vector control technology. For the grid voltage of  $U_s$  during normal operation, in the grid voltage vector control mode, when the voltage drop depth is  $h$ , the relationship between the output power of the DFIG stator and the AC side current of the RSC can be shown as [19]:

$$\begin{cases} P_s = \frac{3L_m}{2L_s} (1-h)U_s i_{rd} \\ Q_s = -\frac{3U_s(1-h)}{2\omega_s L_s} (U_s(1-h) + \omega_s L_m i_{rq}) \end{cases} \quad (12)$$

where  $P_s$  is the stator output active power,  $Q_s$  is the stator output reactive power,  $i_{rd}$  is the d-axis component of the rotor current, and  $i_{rq}$  is the q-axis component of the rotor current.

From (12), the power constraint equation of the DFIG stator can be obtained under the constraint of the RSC current  $I_{rmax}$ :

$$\begin{cases} I_r = \sqrt{\left(\frac{2L_s P_s}{3L_m U_s(1-h)}\right)^2 + \left(\frac{2L_s Q_s}{3L_m U_s(1-h)} + \frac{U_s(1-h)}{\omega_s L_m}\right)^2} \\ I_r \leq I_{rmax} \end{cases} \quad (13)$$

The relationship between the output active power of the DFIG stator and the total output power of the DFIG is [35]:

$$P_s = \frac{P_{DFIG}}{1-s} \quad (14)$$

Thus, when the total active power output ( $P_{DFIG}$ ) of the DFIG is 0, the stator can output the maximum reactive power, so the limit of the reactive current output of the stator is:

$$i_{sqmax} = \frac{L_m}{L_s} I_{rmax} - \frac{(1-h)U_s}{L_s \omega_s} \quad (15)$$

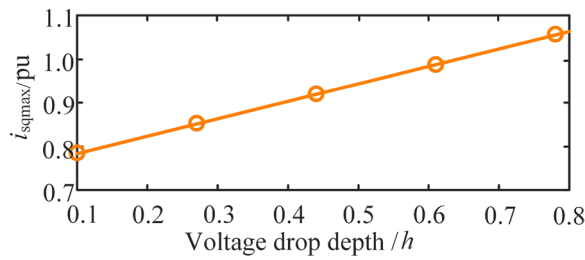


**Fig. 6** Reactive current output capacity of DFIG stator

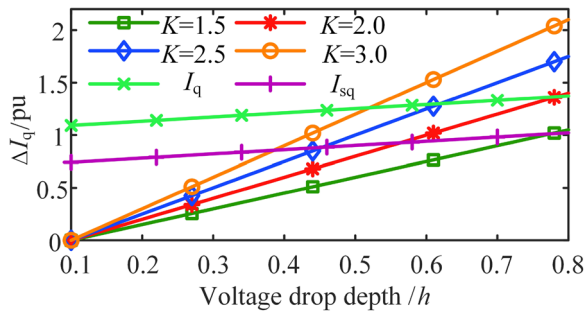


**Fig. 7** DFIG reactive power compensation area

As can be seen from (15), the DFIG stator output reactive current capacity is related to the allowable maximum current  $I_{rmax}$  flowing through the RSC and the voltage drop depth  $h$ . Taking the DFIG parameters in the appendix into (15), under the limit of  $I_{rmax}=1.2pu$ , the relationship between the maximum reactive current output capacity of stator and voltage drop depth  $h$  is obtained, as shown in Fig. 6.

As shown in Fig. 6, the DFIG stator output reactive current capacity is higher than the GSC (0.3 pu), and the stator reactive current output capacity increases with the rise of voltage drop depth  $h$ . When the stator active output is 0 and the voltage drop depth  $h$  is 0.8, the stator reactive current output capacity is the highest at around 1.05 pu.

- (3) Reactive current support and system reactive power demand in wind farms.

According to the analysis in Sects. 3.2.1 and 3.2.2, when the voltage drop depth  $h$  is 0.8 and the priority is given to ensure the reactive output (i.e., the total active output  $P_{DFIG}$  is 0), the DFIG output reactive current capacity is the sum of the stator and GSC output reactive current capacities, at around 1.35 pu. Thus, it can meet the LVRT scenario with a small compensation coefficient  $K$ . Figure 7 shows the amount of reactive current compensation required by the system at different voltage drop

depths  $h$  when the reactive power compensation coefficient  $K=1.5, 2, 2.5, 3$ , and the maximum total reactive current  $I_q$  that the DFIG can provide and the maximum reactive current  $I_{sq}$  that the DFIG stator can provide at different voltage drop depths  $h$ .

It can be seen from Fig. 7 that when the reactive power compensation coefficient  $K$  is small, the DFIG's own reactive power compensation capacity can meet the reactive power compensation requirements for LVRT. However, when both the reactive power compensation coefficient  $K$  and the voltage drop depth  $h$  are large, the output reactive current of the DFIG alone cannot meet the requirements of LVRT. At the same time, it can be seen from Fig. 7 that when the voltage drop depth  $h$  is small, the DFIG has a high margin to output active current because of the small reactive current demand of the system.

As for wind farms without STATCOM, the reactive current can only be supported by the DFIG, and the reactive compensation capability is weak. It can only meet the scenarios with a small reactive compensation coefficient, so the reactive current compensation coefficient  $K$  can be set to 1.5. For DFIG wind farms equipped with STATCOM, both STATCOM and the DFIG can provide reactive current support. With reference to the STATCOM capacity configured for the DFIG wind farm in [36], the maximum reactive current output of the STATCOM is set to 1 pu, so the reactive compensation capacity is high, and the reactive compensation coefficient  $K$  can be increased to 2 or higher to improve the LVRT capacity of the wind farms.

### 3.3 The method of DFIG low voltage ride through

- (1) The crowbar protection switching strategy.

From the analysis of rotor transient characteristics in Sect. 2.2, when the voltage drop depth  $h$  is large, the RSC cannot provide enough voltage to offset the rotor-side induced electromotive force at the initial stage of the fault. This will cause overcurrent at the rotor side. To protect the converter from damage, it is necessary to install a crowbar to protect the circuit. The structure of the crowbar circuit is shown in Fig. 1. During the operation of crowbar protection, the DFIG is in an asynchronous operational state, and the induced electromotive force at the rotor side decays rapidly. When it decays to a reasonable range, the crowbar circuit is disabled, and the RSC restores the power control to the DFIG. Considering whether the crowbar protection is in operation or not, the LVRT process can be divided into two stages: crowbar protection input and reactive current support.

The short-time overcurrent capacity of power electronic devices is generally limited, e.g., twice the rated

capacity [14, 18]. After considering a certain margin, the crowbar protection scheme in this paper adopts a hysteresis strategy. When the rotor current is detected to be greater than 1.7 pu, the crowbar is put into operation and the RSC is locked. During crowbar operation, when the rotor current becomes lower than 1.5 pu, the crowbar is disabled, and the converter resumes control of the DFIG.

- (1) Study on active and reactive power distribution scheme of wind farms for the LVRT period.

From the previous analysis, wind farms should output as much active current as possible while providing reactive power support. For wind farms equipped with STATCOM, it is preferable to use the STATCOM to output reactive current during the LVRT period. When the output reactive current of the STATCOM does not meet the demand, the DFIG is used to output the reactive current. Therefore, the reactive current  $I_Q$  required for the DFIG during the LVRT period is:

$$I_Q = \begin{cases} 0 & K(0.9 - U_{pcc}) \leq 1 \text{ pu} \\ K(0.9 - U_{pcc}) - 1 & K(0.9 - U_{pcc}) > 1 \text{ pu} \end{cases} \quad (16)$$

where  $U_{pcc}$  is the per unit value of grid voltage at the PCC during the LVRT period, and is given by  $U_{pcc} = U_s(1 - h)$ .

The reactive current of the wind farm without STATCOM can only be provided by the DFIG, so there is:

$$I_Q = K(0.9 - U_{pcc}) \quad (17)$$

From (12) and (14), the total active power output  $P_{DFIG}$  of the DFIG has the following relationship with the rotor current  $i_{rd}$  during the LVRT period:

$$P_{DFIG} = \frac{3L_m}{2L_s}(1 - s)U_{pcc}i_{rd} \quad (18)$$

It can be seen from (18) that the total active power output of the DFIG ( $P_{DFIG}$ ) is maximized when the d-axis current  $i_{rd}$  of the RSC reaches the maximum.

Under the constraint of rotor current  $I_{rmax}$ , the rotor dq-axes currents  $i_{rd}$  and  $i_{rq}$  have the constraint of:

$$i_{rd}^2 + i_{rq}^2 \leq I_{rmax}^2 \quad (19)$$

As can be seen from (19), to maximize the d-axis current  $i_{rd}$  of the RSC, the q-axis current modulus  $|i_{rq}|$  should be as small as possible to meet the requirements.

The reactive current of the DFIG during the LVRT period is provided by both the GSC and the DFIG stator:

$$I_Q = i_{gq} + i_{sq} \quad (20)$$

where  $i_{gq}$  and  $i_{sq}$  are the reactive currents provided by the GSC and the DFIG stator, respectively.

The relationship between DFIG stator output reactive power  $Q_s$  and stator reactive current  $i_{sq}$  and rotor q-axis current  $i_{rq}$  is given as:

$$Q_s = -\frac{3U_{pcc}}{2\omega_s L_s}(U_{pcc} + \omega_s L_m i_{rq}) = \frac{3}{2}U_{pcc}i_{sq} \quad (21)$$

From (21), the relationship between  $i_{sq}$  and  $i_{rq}$  can be calculated as:

$$i_{sq} = -\frac{1}{\omega_s L_s}(U_{pcc} + \omega_s L_m i_{rq}) \quad (22)$$

From (22), only when the rotor q-axis current  $i_{rq}$  is less than 0 can the DFIG stator output reactive current ( $i_{sq}$  is greater than 0), and the greater the rotor q-axis current modulus  $|i_{rq}|$ , the greater the stator output reactive current  $i_{sq}$ . From (20) and (22), to make the current modulus  $|i_{rq}|$  of the rotor q-axis as small as possible, the GSC should be used first to output reactive current, and then the DFIG stator is used to output reactive current.

The control target of the GSC is the stability of the DC side voltage. The d-axis reference value  $i_{gd\_LVRT}$  of the current loop for the GSC during the LVRT period is obtained from the voltage outer loop, and needs to be guaranteed first, as:

$$i_{gd\_LVRT} = i_{gdref} \quad (23)$$

where  $i_{gdref}$  is the reference value of active current obtained by the DC voltage loop of the GSC.

To ensure that the DFIG can output more active power, the GSC should be preferentially used to output reactive current during the LVRT period, and the q-axis current reference value  $i_{gq\_LVRT}$  can be set to:

$$i_{gq\_LVRT} = \min\left(\sqrt{I_{gmax}^2 - i_{gdref}^2}, I_Q\right) \quad (24)$$

where  $I_{gmax}$  is the maximum current allowed to pass through the GSC, and usually  $I_{gmax}$  is 0.3 pu.

When the reactive current output capacity of the GSC can meet the reactive current demand of the power system, i.e.,  $\sqrt{I_{gmax}^2 - i_{gdref}^2} > I_Q$ , only the GSC provides the reactive current and the DFIG stator does not need to output reactive current (i.e.,  $i_{sq} = 0$ ). From (22), the q-axis reference value  $i_{rq\_LVRT}$  for the current loop of the RSC should be set as follows:

$$i_{rq\_LVRT} = -\frac{U_{pcc}}{\omega_s L_m} \quad (25)$$

To ensure that the DFIG can output as much active power as possible while satisfying the reactive power



needs of the power system, the d-axis reference value  $i_{rd\_LVRT}$  for the current loop of the RSC should be set as:

$$i_{rd\_LVRT} = \min \left( \sqrt{I_{rmax}^2 - i_{rq\_LVRT}^2}, i_{rdref} \right) \quad (26)$$

where  $I_{rmax}$  is the maximum current allowed to pass through the RSC, and usually  $I_{rmax}$  is 1.2 pu.  $i_{rdref}$  is the active current reference value obtained by maximum power tracking control.

When the reactive current output capacity of the GSC cannot meet the reactive current demand of the power system, i.e.,  $\sqrt{I_2^2 g_{max} - i_2^2 g_{dref}} < I_Q$ , the DFIG stator is also required to output reactive current. To prioritize the reactive current output, from (22), the q-axis reference value  $i_{rq\_LVRT}$  for the current loop of the RSC should be set to:

$$i_{rq\_LVRT} = \frac{-U_{pcc}}{\omega_s L_m} - \frac{L_s (I_Q - i_{gq\_LVRT})}{L_m} \quad (27)$$

To meet the reactive power demand of the system, and to ensure that the DFIG can output the maximum active power, the d-axis reference value  $i_{rd\_LVRT}$  for the current loop of the RSC is still given by (26).

Wind farms equipped with STATCOM can increase the value of  $K$  to be higher than 2 to enhance the LVRT capability. From (23–27), the reference value of the current loop of the STATCOM, GSC, and RSC during the LVRT period can be as given in Fig. 8.

Wind farms without STATCOM set the value of  $K$  to 1.5. From (23–27), the reference value of the current loop of the GSC and RSC during the LVRT period is given by the block diagram shown in Fig. 9.

When adopting the reactive current distribution strategies shown in Figs. 8 and 9 during the LVRT period, the DFIG wind farm has the ability to output more active power while meeting the national standard GB/T 19963.1-2021 reactive current support. This slows down the rising rate of rotor speed and improves the LVRT operation capability of the wind farm.

#### 4 Simulation analysis of the DFIG's low voltage ride through strategy

To verify the effectiveness of the LVRT scheme proposed, a DFIG wind turbine model as shown in Fig. 1 is constructed on the PSCAD/EMTDC simulation platform. The simulation parameters are detailed in the Appendix. The reactive current compensation coefficient  $K$  for the wind farm equipped with STATCOM is set to 2.5, while for the wind farm without STATCOM it is set to 1.5. To better simulate the actual operating conditions of the wind farms and to satisfy the LVRT curve in Fig. 5, three fault scenarios

are designed in this paper, and the proposed scheme is compared with traditional crowbar protection schemes in [11, 12].

*Scenario 1* The wind farm is operating normally at rated power when a fault occurs at 2 s, causing a voltage drop of depth  $h=0.3$ . The fault lasts for 1.608 s.

*Scenario 2* The wind farm is operating normally at rated power when a fault occurs at 2 s, causing a voltage drop of depth  $h=0.8$ . The fault lasts for 0.625 s.

*Scenario 3* The wind farm is operating at 40% of the rated power when a fault occurs at 2 s, causing a voltage drop of depth  $h=0.8$ . The fault lasts for 0.625 s.

Figure 10 shows the voltage at the PCC ( $U_l$ ), the rotor current magnitude ( $I_{rmag}$ ), the total reactive current output of the wind farm ( $I_Q$ ), the total DFIG reactive power output ( $Q_{DFIG}$ ), the total DFIG active power output ( $P_{DFIG}$ ), and the slip rate  $s$  in Scenario 1.

From Fig. 10a, d, it can be seen that the grid voltage drops to 0.7 pu when no LVRT measures are taken by the wind farm. The traditional crowbar protection scheme causes the DFIG to absorb a large amount of reactive power for excitation, further reducing the grid voltage to 0.605 pu. From Fig. 10e, f, it can be seen that the traditional crowbar protection scheme cannot effectively control the output power of the DFIG through the RSC, resulting in a decrease in the DFIG's active power output. At this time, the wind turbine's input mechanical power is greater than the output electromagnetic power, causing the DFIG rotor speed to increase and the slip rate to decrease. For the proposed method, it can be seen from Fig. 10b that the crowbar protection scheme does not activate because the depth of voltage drop is small, and the rotor-side current does not exceed the limit. In the case of the wind farm without STATCOM, the DFIG stator and GSC jointly provide 0.262 pu reactive current, as shown in Fig. 10d, of which 0.09 pu is provided by the GSC and 0.172 pu is provided by the DFIG stator. With the support of reactive current, the grid voltage increases to 0.726 pu, as shown in Fig. 10a. The wind farm equipped with STATCOM only relies on STATCOM to provide 0.41 pu reactive current, as shown in Fig. 10c, while the DFIG no longer provides reactive power support. With the support of reactive power from the STATCOM, the grid voltage rises to 0.736 pu, as shown in Fig. 10a. From Fig. 10e, f, it can be seen that the proposed method has good LVRT capability when the depth of voltage drop is small, and the DFIG can output active power to the grid with only small changes in the wind turbine rotor speed and slip rate.

Figure 11 shows the voltage at the PCC ( $U_l$ ), the rotor current magnitude ( $I_{rmag}$ ), the total reactive current output of the wind farm ( $I_Q$ ), the total DFIG reactive power

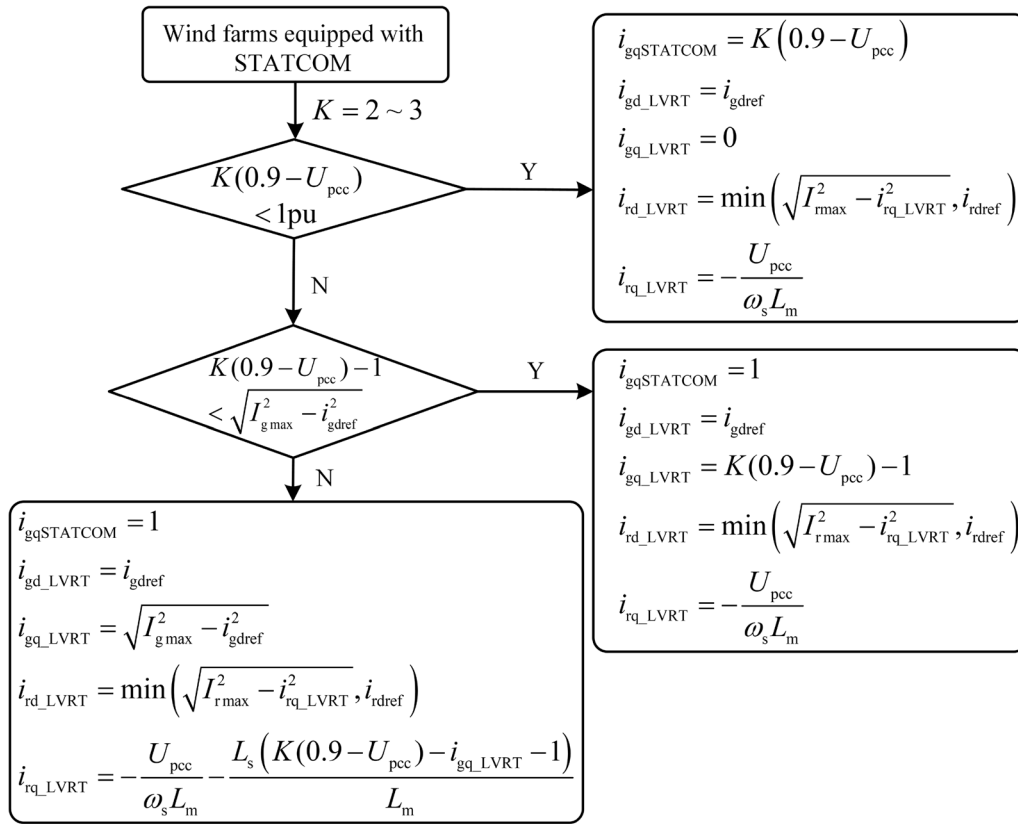


**Fig. 8** Reactive current distribution strategy of wind farms equipped with STATCOM

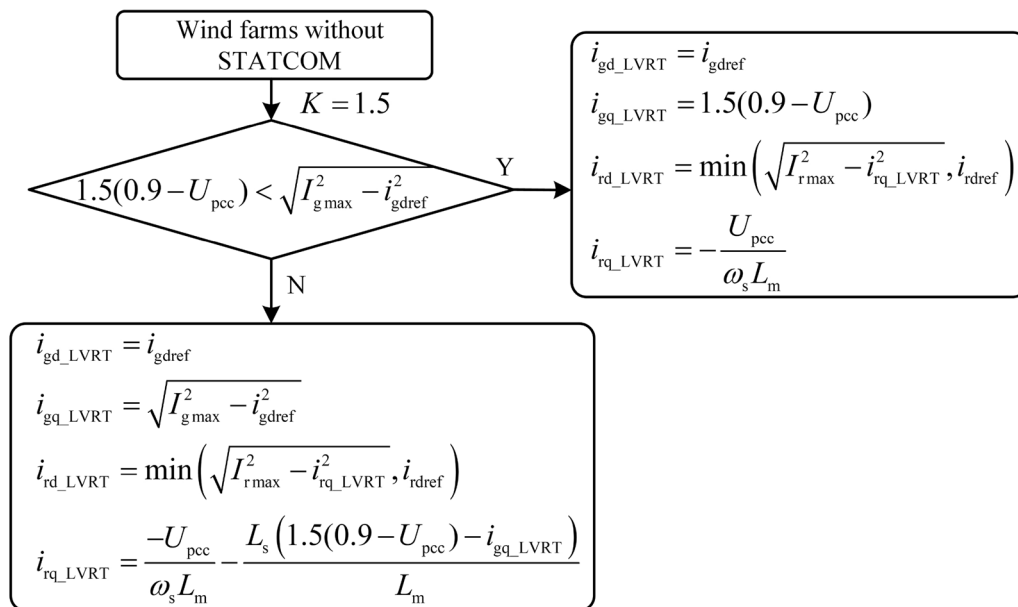


**Fig. 9** Reactive current distribution strategy of wind farms without STATCOM

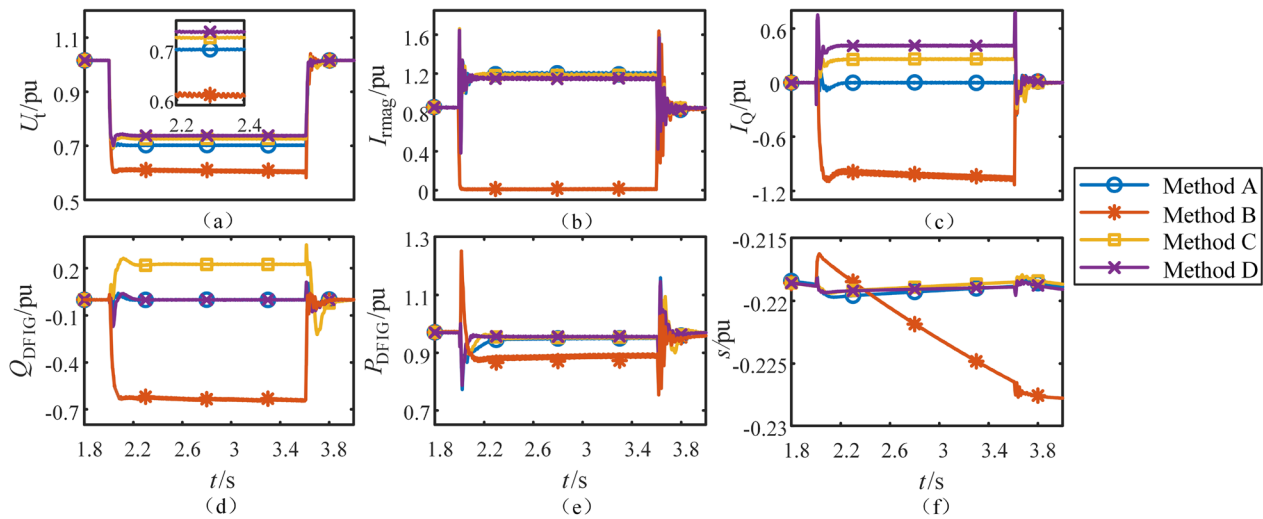


**Fig. 10** Simulation results of LVRT for the wind farm in Scenario 1. **a** is the voltage at the PCC; **b** is the rotor current magnitude; **c** is the total reactive current output; **d** is the total DFIG reactive power; **e** is the total DFIG active power; **f** is the slip rate

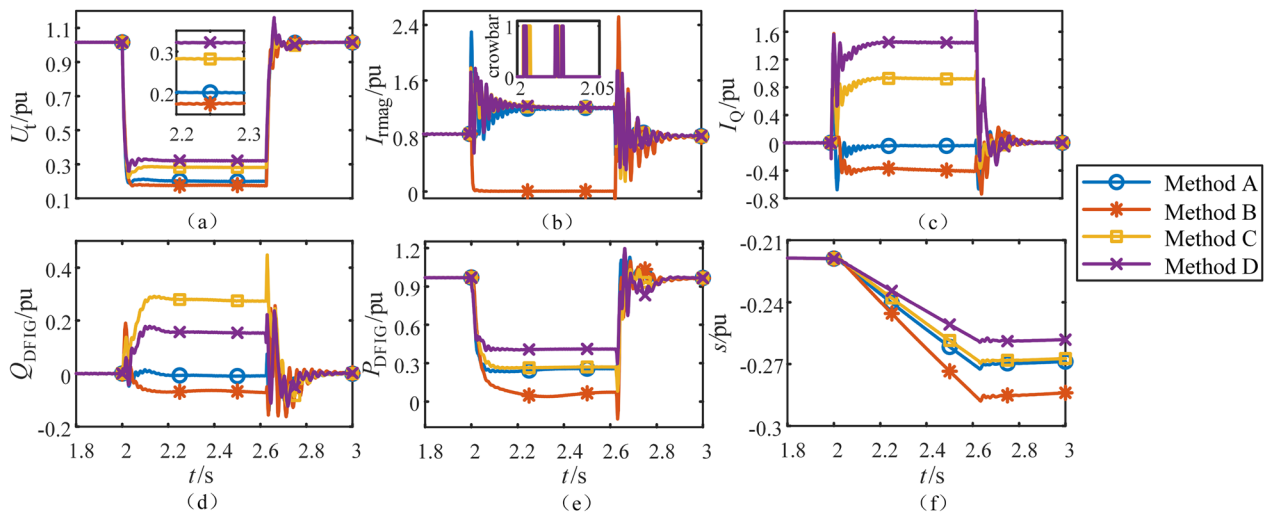
output ( $Q_{\text{DFIG}}$ ), the total DFIG active power output ( $P_{\text{DFIG}}$ ), and the slip rate ( $s$ ) in Scenario 2.

It can be seen from Fig. 11a that when the wind farm does not take any LVRT measures, the DFIG rotor current magnitude  $I_{\text{rmag}}$  exceeds 2 pu when the voltage at the PCC drops to 0.2 pu, as shown in Fig. 11b. This can cause damage to the DFIG converter. For the traditional crowbar protection scheme, Fig. 11d shows that the DFIG absorbs a large amount of reactive power from the system, causing the voltage at the PCC to drop further to 0.162 pu. Also, because of the voltage drop and the inability of the RSC to effectively control the DFIG output power, the active power output of the DFIG is reduced. For the proposed scheme, it can be seen from Fig. 11b that when the crowbar circuit is switched in accordance with the hysteresis strategy, the RSC current can be limited within 1.7 pu, and the converter can recover control of DFIG within 50 ms. The wind farm without STATCOM relies on the reactive current of DFIG to provide 0.93 pu, as shown in Fig. 11c, where the DFIG stator provides 0.70–0.71 pu reactive current and the GSC provides 0.23–0.22 pu reactive current. With the support of the reactive current, the voltage at the PCC is increased to 0.28 pu, as shown in Fig. 11a. The wind farm equipped with STATCOM provides 1.44 pu reactive current jointly from the DFIG and STATCOM, as shown in Fig. 11c, where the STATCOM provides 1 pu, the DFIG stator provides 0.25–0.27 pu, and the GSC provides 0.19–0.17 pu. At this time, the voltage at the PCC is increased to 0.32 pu, as shown in Fig. 11a. It can be seen from Fig. 11e, f that when the voltage at the PCC drops significantly, the active power output of the DFIG is less than the input mechanical power. This causes the rotor speed of

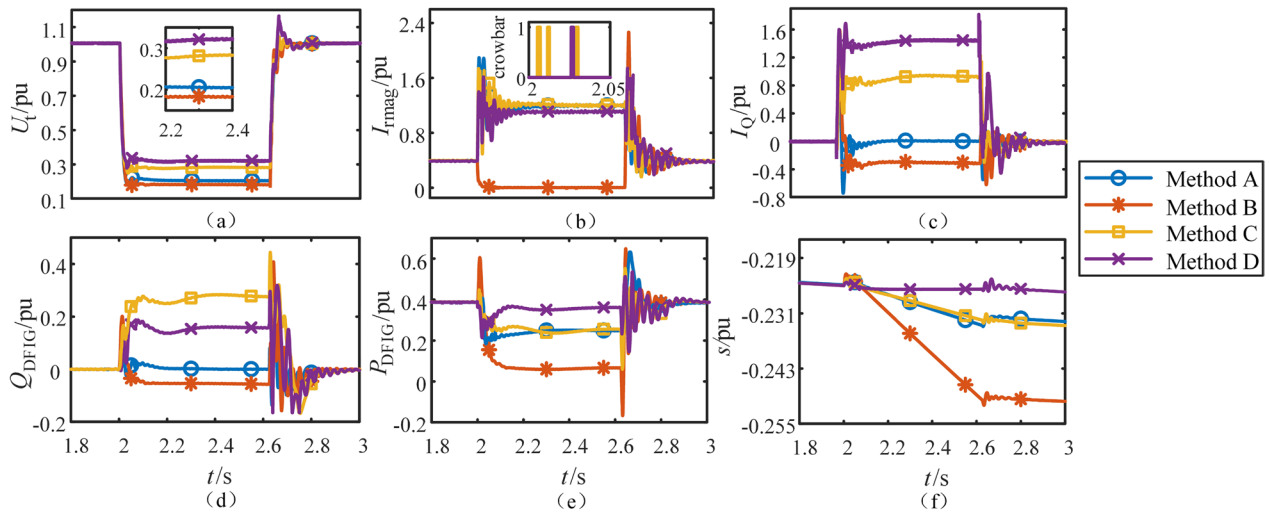
the wind turbine to increase rapidly and the slip rate to change greatly. Compared with the wind farm without STATCOM, the wind farm equipped with STATCOM can provide more active power output, the rotor speed increases slower, and the LVRT capability is better.

Figure 12 shows the voltage at the PCC ( $U_t$ ), the rotor current magnitude ( $I_{\text{rmag}}$ ), the total reactive current output of the wind farm ( $I_Q$ ), the total DFIG reactive power output ( $Q_{\text{DFIG}}$ ), the total DFIG active power output ( $P_{\text{DFIG}}$ ), and the slip rate  $s$  in Scenario 3.

From Fig. 12a, when no LVRT measures are taken by the wind farm, the grid voltage drops to 0.2 pu. Figure 12d shows that the traditional crowbar protection scheme causes the DFIG to absorb reactive power from the system, causing the grid voltage to further drop to 0.175 pu. At the same time, the DFIG active power output decreases, causing the DFIG rotor speed to increase. For the proposed scheme, it can be seen from Fig. 12b that the rotor over-current can be effectively limited by using the crowbar, and the converter can quickly recover control of the DFIG. The wind farm without STATCOM relies on the DFIG to provide 0.93 pu reactive current, as shown in Fig. 12c, where the DFIG stator provides 0.70 pu and the GSC provides 0.23 pu. With the support of the reactive current, the grid voltage is raised to 0.28 pu, as shown in Fig. 12a. In the wind farm equipped with STATCOM, the DFIG and STATCOM jointly provide 1.44 pu reactive current, as shown in Fig. 12c, where the STATCOM provides 1 pu, the DFIG stator provides 0.23 pu, and the GSC provides 0.21 pu. At this point, the grid voltage is raised to 0.32 pu, as shown in Fig. 12a. From Fig. 12e, f, it can be seen that when the depth of the grid voltage drop is large, the DFIG output active power will



**Fig. 11** Simulation results of LVRT for the wind farm in Scenario 2. **a** is the voltage at the PCC; **b** is the rotor current magnitude; **c** is the total reactive current output; **d** is the total DFIG reactive power; **e** is the total DFIG active power; **f** is the slip rate



**Fig. 12** Simulation results of LVRT for the wind farm in Scenario 3. **a** is the voltage at the PCC; **b** is the rotor current magnitude; **c** is the total reactive current output; **d** is the total DFIG reactive power; **e** is the total DFIG active power; **f** is the slip rate

be limited. In contrast to Scenario 2, where the wind farm operates at rated power, the wind farm operates at only 40% of the rated power in Scenario 3, so the difference between the DFIG input mechanical power and the output electromagnetic power is relatively small, and the wind turbine rotor speed rises more slowly. For the wind farm equipped with STATCOM, it can even fully output the generated active power, and the change in rotor speed is thus insignificant.

From the LVRT simulation results for the wind farms under Scenarios 1–3, it is found that both the proposed scheme and the traditional crowbar protection scheme can effectively limit the rotor current and avoid

large-scale disconnection of wind turbines during faults. However, the traditional crowbar protection scheme absorbs a large amount of reactive power for excitation during the operation of the crowbar circuit, causing a further drop in the grid voltage at the PCC and failing to meet the requirement of reactive current support in the standard. In contrast, the proposed scheme can output reactive current according to the standard during LVRT, effectively supporting the recovery of the grid voltage at the PCC. Additionally, when the voltage drop is high, the traditional crowbar protection scheme cannot effectively control the DFIG output power because of the RSC being locked, resulting in a significant reduction

in its output active power and a rapid increase in the DFIG rotor speed. In contrast, the proposed scheme can quickly recover the control of the DFIG through RSC and maintain its output power, thereby suppressing the rate of rotor speed increase to some extent and improving the LVRT capability of the wind farm. In summary, compared to the traditional crowbar protection scheme, the proposed scheme has better performance in limiting rotor overcurrent and controlling reactive power and active power outputs, thus improving the LVRT capability of the wind farm.

## 5 Conclusion

To enhance the LVRT capability of DFIG wind farms during symmetrical faults, this paper considers the reactive and active current output capabilities of wind farms whether or not wind farms are equipped with STATCOM. While satisfying the standard requirements for reactive current output, an optimized scheme for allocating reactive and active currents during LVRT is proposed. The main contributions and innovations of this paper are as follows:

1. Revealing the relationship between the limit of the reactive current output of DFIG and the depth of voltage drop. Through research on the current constraints of the converter, it is shown that the reactive current output limit of the GSC is independent of the depth of voltage drop, and its limit is the maximum current allowed by the converter, which is around 0.3 pu. The reactive current output limit of the DFIG stator is a linear function of the depth of voltage drop, and the slope of the function is positive, while the specific value is related to the internal parameters of the DFIG.
2. Proposing an optimized scheme for allocating reactive and active currents among the STATCOM, DFIG stator, and GSC during the LVRT period. Unlike traditional LVRT strategies that only focus on the reactive current output, the proposed scheme considers the impact of active current output on LVRT performance. By ensuring that the reactive current output of the wind farm meets the standard requirements while maximizing the active current output, this scheme can better suppress the rate of rotor speed increase and enhance the LVRT performance and fault recovery capability of wind farms.

The results provide useful ideas and methods for improving the LVRT capability of DFIG wind farms. In the future, we will continue to conduct in-depth research on the zero voltage ride-through (ZVRT) scheme of DFIG wind farms, a LVRT scheme under asymmetric

faults, and LVRT optimization scheme for other types of wind farms.

## Appendix 1

The main parameters of the DFIG used in this paper are as follows: the rated power is 5 MW; the system frequency is 50 Hz; the rated voltage of PCC is 690 V; the stator resistance  $R_s$  is 0.0054 pu; the stator inductance  $L_s$  is 2.5 pu; The excitation inductance  $L_m$  is 2.4 pu; The rotor resistance  $R_r$  is 0.00607 pu; The rotor inductance  $L_r$  is 2.51 pu; The maximum output reactive current of STATCOM is 1 pu.

### Abbreviations

DFIG	Doubly-fed induction generator
LVRT	Low voltage ride-through
ZVRT	Zero voltage ride-through
PMSG	Permanent magnet synchronous generator
PCC	Point of common coupling
RSC	Rotor side converter
GSC	Grid side converter
STATCOM	Static synchronous compensator
SVC	Static var compensator

### List of symbols

$\mathbf{U}_s^r$	Stator voltage vector in the rotor coordinate system
$R_s$	Resistance of DFIG stator
$\mathbf{I}_s^r$	Stator current vector in the rotor coordinate system
$\boldsymbol{\Psi}_s^r$	Stator flux vector in the rotor coordinate system
$\omega_r$	Rotor speed
$\mathbf{U}_r^r$	Rotor voltage vector in the rotor coordinate system
$R_r$	Resistance of DFIG rotor
$\omega_s$	Synchronous speed
$\omega_{\text{slip}}$	Slip speed, $\omega_{\text{slip}} = \omega_s - \omega_r$
$\mathbf{I}_r^r$	Rotor current vector in the rotor coordinate system
$\boldsymbol{\Psi}_r^r$	Rotor flux vector in the rotor coordinate system
$L_m$	Excitation inductance
$L_s$	Inductance of DFIG stator
$L_r$	Inductance of DFIG rotor
$\sigma$	Magnetic leakage coefficient, $\sigma = 1 - L_m^2 / (L_r L_s)$
$\mathbf{E}_r$	Induced electromotive force at the rotor side
$U_s$	Grid voltage modulus during normal operation
$U_{\text{dc}}$	DC voltage of the converters
$P_s$	Active power of the stator
$P_g$	Active power of the grid-side converter
$Q_s$	Reactive power of the stator
$Q_g$	Reactive power of the grid-side converter
$s$	Rate of slip, $s = (\omega_r - \omega_s) / \omega_s$
$T_s$	Stator time constant, $T_s = L_s / R_s$
$E_{r\text{max}}$	Maximum value of the rotor side induced electromotive force
$\Delta I_q$	Reactive current increment
$K$	Reactive compensation coefficient
$U_{\text{pcc}}$	Unit value of the PCC voltage
$I_N$	Rated current of wind farm
$I_{g\text{max}}$	Maximum current allowed through the grid-side converter
$P_{\text{DFIG}}$	Total output active power of DFIG
$i_{gd}$	d-Axis component of the grid-side converter current
$i_{gq}$	q-Axis component of the grid-side converter current
$i_{rd}$	d-Axis component of the rotor current
$i_{rq}$	q-Axis component of the rotor current
$I_{r\text{max}}$	Maximum current allowed through the rotor-side converter
$I_Q$	Reactive current required for output by DFIG during the LVRT period
$i_{sq}$	Reactive current provided by the DFIG stator



$i_{gd\_LVRT}$	d-Axis reference value of the current loop for the GSC during the LVRT period
$i_{gref}$	Reference value of active current obtained by the voltage loop of the GSC
$i_{gq\_LVRT}$	q-Axis reference value of the current loop for the GSC during the LVRT period
$i_{rd\_LVRT}$	d-Axis reference value of the current loop for the RSC during the LVRT period
$i_{rq\_LVRT}$	q-Axis reference value of the current loop for the RSC during the LVRT period
$i_{gq\_STATCOM}$	Reactive current reference value of STATCOM during the LVRT period

### Acknowledgements

This research was funded by grants from the National Natural Science Foundation of China (52177108).

### Author contributions

BL as the first author, contributed significantly to the analysis and research of the paper. DZ contributed significantly to the research and writing of the paper. BL contributed to the submission of the paper and helped to improve the paper's quality. XJ, QH, and LJ also helped to revise the manuscript. All the authors read and approved the submitted manuscript.

### Funding

This work was supported by the National Natural Science Foundation of China 52177108.

### Availability of data and materials

Data and materials are obtained simulation program. This simulation program is PSCAD/EMTDC.

### Declarations

### Competing interests

The authors declare that they have no known competing financial interests or personal relationships that could have appeared to influence the work reported in this paper.

Received: 16 February 2023 Accepted: 7 July 2023

Published online: 27 July 2023

### References

- Karakurt, I., Aydin, G., Kaya, S., & Hamzacebi, C. (2015). Forecasting of Turkey's coal consumption using grey prediction technique. In *24th International Mining Congress and Exhibition of Turkey, Antalya, Turkey*, pp. 78–82.
- Geng, H., Liu, C., & Yang, G. (2013). LVRT capability of DFIG-based WECS under asymmetrical grid fault condition. *IEEE Transactions on Industrial Electronics*, 60(6), 2495–2509.
- Mohseni, M., Islam, S., & Masoum, M. (2011). Impacts of symmetrical and asymmetrical voltage sags on DFIG-based wind turbines considering phase-angle jump, voltage recovery, and sag parameters. *IEEE Transactions on Power Electronics*, 26(5), 1587–1598.
- Ling, Y. (2012). Transient characteristics analysis of DFIG-based wind turbine under symmetrical fault. *Proceedings of the CSEE*, 42(18), 6871–6880.
- Mosayyebi, S. R., Shahalami, S. H., & Mojallali, H. (2022). Fault ride-through capability improvement in a DFIG-based wind turbine using modified ADRC. *Protection and Control of Modern Power Systems*, 7(1), 50.
- Kartjokolaie, H. S., Radmehr, M., & Firouzi, M. (2018). LVRT capability enhancement of DFIG-based wind farms by using capacitive DC reactor-type fault current limiter. *International Journal of Electrical Power & Energy Systems*, 102, 287–295.
- Hiremath, R., & Moger, T. (2022). Modified Super Twisting algorithm based sliding mode control for LVRT enhancement of DFIG driven wind system. *Energy Reports*, 8, 3600–3613.
- Zhang, Y., Liu, J. H., Zhou, M. L., Li, C., & Lv, Y. L. (2022). Double impedance-substitution control of DFIG Based wind energy conversion system. *Energies*, 15(15), 5739.
- Li, S. L., Wang, W. S., Wang, R. M., Sun, Y., & Chen, C. (2016). Control strategy and experiment of high voltage ride through for DFIG-based wind turbines. *Automation of Electric Power Systems*, 40(16), 76–82.
- Mu, G., Wang, J., Yan, G. G., Cui, Y., Huang, Y. F., & An, J. (2011). Cascading Trip-off of doubly-fed induction generators from grid at near full-load condition in a wind farm. *Automation of Electric Power Systems*, 35(22), 35–40.
- Weise, B. (2015). Impact of K-factor and active current reduction during fault-ride-through of generating units connected via voltage-sourced converters on power system stability. *IET Renewable Power Generation*, 9(1), 25–36.
- Technical Specification for Wind Farm Access to Power System Part 1: Onshore Wind Power. (2021). *National Electricity Regulatory Standardization Technical Committee*, GB/T 19963.1-2021.
- Patel, K. S., & Makwana, V. H. (2022). LVRT fulfilment of the DFIG-based WECS during symmetrical grid voltage dips. *IETE Journal of Research*. <https://doi.org/10.1080/03772063.2022.2055658>
- Cheng, H. B., Yuan, W., Zhou, W. B., Xu, J. G., & Lu, R. B. (2013). Design for the LVRT scheme of DFIG based on DBR. *Power System Protection and Control*, 41(13), 122–128.
- Xu, D. G., Wang, W., & Chen, N. (2010). Dynamic characteristic analysis of doubly-fed induction generator low voltage ride-through based on crowbar protection. *Proceedings of the CSEE*, 30(22), 29–36.
- Li, Z. M., Li, W. W., & Pan, T. H. (2016). An optimized compensation strategy of DVR for micro-grid voltage sag. *Protection and Control of Modern Power Systems*, 1(1), 78–85.
- Tan, A. G., Wu, Y. Y., Wang, C. Q., & Li, F. Y. (2021). Adaptive switching strategy for a wind turbine crowbar based on the guarantee of low voltage ride-through capability. *Power System Protection and Control*, 49(18), 98–109.
- Jiang, H. L., Fan, Z. L., & Chen, J. (2018). Low voltage ride-through method of DFIG based wind turbines by dynamically adjusting crowbar resistance of rotor. *Automation of Electric Power Systems*, 42(1), 125–131.
- Sun, L. N., & Wang, Y. J. (2018). LV ride through control strategy of doubly fed induction generator based on crowbar series capacitor. *Power System Technology*, 42(7), 2089–2094.
- Zou, X. D., Zhu, D. H., Hu, J. B., Zhou, S. Y., & Kang, Y. (2018). Mechanism analysis of the required rotor current and voltage for DFIG-based WTs to ride-through severe symmetrical grid faults. *IEEE Transactions on power electronics*, 33(9), 7300–7304.
- Cheng, P., Nian, H., & Chu, Z. Q. (2014). Control technique of DFIG based on virtual resistance under symmetrical grid fault. *Electric Machines and Control*, 18(6), 1–8.
- Zhu, D., Zou, X., Deng, L., Huang, Q., Zhou, S., & Kang, Y. (2016). Inductance-emulating control for DFIG-based wind turbine to ride-through grid faults. *IEEE Transactions on power electronics*, 32(11), 8514–8525.
- Sun, P., Yao, J., Liu, R. K., Pei, J. X., Zhang, H. L., & Liu, Y. (2021). Virtual capacitance control for improving dynamic stability of the DFIG-based wind turbines during a symmetrical fault in a weak AC grid. *IEEE Transactions on Industrial Electronics*, 68(1), 333–346.
- Yang, G. S., Wang, Z. P., Ouyang, J. X., Wang, X. Y., Zheng, D., & Xiong, X. F. (2018). Short-circuit current calculation method of DFIGWT considering entire LVRT process. *Power System Technology*, 42(7), 2185–2193.
- Li, H., Fu, B., Yang, C., Zhao, B., & Tang, X. F. (2012). Reactive current allocation and control strategies improvement of low voltage ride through for doubly fed induction wind turbine generation system. *Proceedings of the CSEE*, 32(22), 24–31.
- Arun Kumar, P. K., & Kannan, S. M. (2016). Low voltage ride through capability improvement in a grid connected wind energy conversion system using STATCOM. In *International Conference on Energy Efficient Technologies for Sustainability, Nagercoil, India*, pp. 603–608.
- Rezaie, H., & Kazemi-Rahbar, M. H. (2019). Enhancing voltage stability and LVRT capability of a wind-integrated power system using a fuzzy-based SVC. *Engineering Science and Technology-an International Journal-Jestech*, 22(3), 827–839.
- Amalorpavaraj, R. A. J., Kaliannan, P., Padmanaban, S., Subramaniam, U., & Ramachandaramurthy, V. K. (2017). Improved fault ride through capability

- in DFIG based wind turbines using dynamic voltage restorer with combined feed-forward and feed-back control. *IEEE Access*, 5, 20494–20503.
29. Mahdianpoor, F. M., Hooshmand, R. A., & Ataei, M. (2018). A New approach to multifunctional dynamic voltage restorer implementation for emergency control in distribution systems. *IEEE Transactions on Power Delivery*, 26(2), 882–890.
  30. Liserre, M., Cardenas, R., Molinas, M., & Rodriguez, J. (2015). Impacts of high penetration of DFIG Wind turbines on rotor angle stability of power systems. *IEEE Transactions on Sustainable Energy*, 6(3), 759–766.
  31. Edrah, M., Lo, K. L., & Lare, O. A. (2011). Overview of multi-MW wind turbines and wind parks. *IEEE Transactions on Industrial Electronics*, 58(4), 1081–1095.
  32. Mensou, S., Essadki, A., & Nasser, T. (2020). A direct power control of a DFIG based-WECS during symmetrical voltage dips. *Protection and Control of Modern Power Systems*, 5(1), 5.
  33. Cui, J., Gao, X., Xie, Z., & Xu, K.B. (2021). Fault ride-through control strategy of doubly-fed wind turbine under symmetrical grid faults. In *16th IEEE Conference on Industrial Electronics and Applications, Chengdu, China*, pp. 572–576.
  34. Yang, R. H., & Jin, J. X. (2020). Unified power quality conditioner with advanced dual control for performance improvement of DFIG-based wind farm. *IEEE Transactions on Sustainable Energy*, 12(1), 116–126.
  35. Lang, Y. Q., Zhang, X. G., Xu, D. G., Ma, H. F., & Hadianmrei, S. R. (2007). Reactive power analysis and control of doubly fed induction generator wind farm. *Proceedings of the CSEE*, 27(9), 77–82.
  36. Zheng, C., Yang, G., & Geng, H. (2013). A control strategy for doubly-fed induction generator based wind farms equipped with STATCOM under asymmetrical grid fault situations. *Proceedings of the CSEE*, 33(9), 27–38.

**Botong Li** The author was born in Baoding, China. He received the B.S., M.S., and Ph.D. degrees in electrical engineering from Tianjin University, Tianjin, China, in 2004, 2007, and 2010, respectively. From 2010 to 2014, he was a Lecturer with the School of Electrical Engineering and Automation, Tianjin University. From 2013 to 2014, he was an R&D Engineer with the Innovation and Technology Department, Alstom Grid U.K. Ltd. Since 2014, he has been an Associate Professor with the School of Electrical and Information Engineering, Tianjin University. He holds ten patents and has authored and coauthored more than 40 papers. He was responsible for more than ten national or provincial projects. His current research focuses on protection and control of dc and ac power systems.

**Dingchuan Zheng** The author was born in Mianyang, China. He received the B.E. degree in electrical engineering in 2021 from Tianjin University, Tianjin, China, where he is currently working toward the M.S. degree in electrical engineering. His current research focuses on the operation and control of new energy power system.

**Bin Li** The author received the B.S., M.S., and Ph.D. degrees in electrical engineering from Tianjin University, Tianjin, China, in 1992, 2002, and 2005, respectively. He is currently a Professor with the School of Electrical Engineering and Automation, Tianjin University. His current research focuses on protection and control of power systems and microgrids.

**Xinru Jiao** The author was born in Nanyang, China. She received a B.E. degree in electrical engineering in 2020 from Tianjin University, Tianjin, China, where she is currently working toward an M.S. degree in electrical engineering. Her current research focuses on the operation and control of new energy power system.

**Qiteng Hong** The author is currently a Chancellor's Fellow at the University of Strathclyde, Glasgow, U.K. His main research interest is in power system protection. He received his Ph.D. degree in Electronic and Electrical Engineering in 2015, from the University of Strathclyde.

He is a Regular Member of the CIGRE Working Group B5.50, IEEE Working Group P2004.

**Liang Ji** The author received his B.Eng. and Ph.D. degrees from the University of Strathclyde, UK. He is presently an Associate Professor in the College of Electrical Engineering at Shanghai University of Electric Power, Shanghai. His research interests include the modeling and simulation of power systems, power system protection, and control.

**Submit your manuscript to a SpringerOpen<sup>®</sup> journal and benefit from:**

- Convenient online submission
- Rigorous peer review
- Open access: articles freely available online
- High visibility within the field
- Retaining the copyright to your article

---

Submit your next manuscript at ► [springeropen.com](https://www.springeropen.com)